Noise Correlations in a Coulomb-Blockaded Quantum Dot

Yiming Zhang,[1] L. DiCarlo,[1] D. T. McClure,[1] M. Yamamoto,[2,3] S. Tarucha,[2,4] C. M. Marcus,[1] M. P. Hanson,[5] and A. C. Gossard[5]

[1]*Department of Physics, Harvard University, Cambridge, Massachusetts 02138, USA*
[2]*Department of Applied Physics, University of Tokyo, Bunkyoku, Tokyo 113-8656, Japan*
[3]*SORST-JST, Kawaguchi-shi, Saitama 331-0012, Japan*
[4]*ICORP-JST, Atsugi-shi, Kanagawa 243-0198, Japan*
[5]*Department of Materials, University of California, Santa Barbara, California 93106, USA*

(Received 14 March 2007; published 20 July 2007)

We report measurements of current noise auto- and cross correlation in a tunable quantum dot with two or three leads. As the Coulomb blockade is lifted at finite source-drain bias, the autocorrelation evolves from super- to sub-Poissonian in the two-lead case, and the cross correlation evolves from positive to negative in the three-lead case, consistent with transport through multiple levels. Cross correlations in the three-lead dot are found to be proportional to the noise in excess of the Poissonian value in the limit of weak output tunneling.

DOI: 10.1103/PhysRevLett.99.036603 PACS numbers: 72.70.+m, 73.21.La

Considered individually, Coulomb repulsion and Fermi statistics both tend to smooth electron flow, thereby reducing shot noise below the uncorrelated Poissonian limit [1,2]. For similar reasons, Fermi statistics without interactions also induces a negative noise cross correlation in multiterminal devices [1–4]. It is therefore surprising that, under certain conditions, the interplay between Fermi statistics and Coulomb interaction can lead to electron bunching, i.e., super-Poissonian autocorrelation and positive cross correlation of electronic noise.

The specific conditions under which such positive noise correlations can arise has been the subject of numerous theoretical [5–14] and experimental [14–23] studies in the past few years. Super-Poissonian noise observed in metal-semiconductor field effect transistors [15], tunnel barriers [16], and self-assembled stacked quantum dots [17] has been attributed to interacting localized states [10,15,24] occurring naturally in these devices. In more controlled geometries, super-Poissonian noise has been associated with inelastic cotunneling [9] in a nanotube quantum dot [20] and with dynamical channel blockade [11,12] in GaAs/AlGaAs quantum dots in the weak-tunneling [21] and quantum Hall regimes [22]. Positive noise cross correlation has been observed in a capacitively coupled double dot [23] as well as in electronic beam splitters following either an inelastic voltage probe [5–8,19] or a super-Poissonian noise source [18]. The predicted positive noise cross correlation in a three-lead quantum dot [12] has not been reported experimentally to our knowledge.

This Letter describes measurement of current noise auto- and cross correlation in a Coulomb-blockaded quantum dot configured to have either two or three leads. As a function of gate voltage and bias, regions of super- and sub-Poissonian noise, as well as positive and negative noise cross correlation, are identified. Results are in good agreement with a multilevel sequential-tunneling model in which electron bunching arises from dynamical channel blockade [11,12]. For weak-tunneling output leads, noise cross correlation in the three-lead configuration is found to be proportional to the deviation of the autocorrelation from the Poissonian value (either positive or negative) similar to the relation found in electronic Hanbury Brown-Twiss (HBT)-type experiments [3,4,18].

The quantum dot is defined by gates on the surface of a $GaAs/Al_{0.3}Ga_{0.7}As$ heterostructure [Fig. 1(a)]. The two-dimensional electron gas 100 nm below the surface has density 2×10^{11} cm^{-2} and mobility 2×10^5 cm^2/V s. Leads formed by gate pairs V_{l}-V_{bl}, V_{r}-V_{br}, and V_{l}-V_{r} connect the dot to three reservoirs labeled 0, 1, and 2, respectively. Plunger gate voltage V_{bc} controls the electron number in the dot, which we estimate to be $\sim$100. The constriction formed by V_{tl}-V_{l} is closed.

A ^{3}He cryostat is configured to allow simultaneous conductance measurement near dc and noise measurement near 2 MHz [25]. For dc measurements, the three reservoirs are each connected to a voltage amplifier, a current source, and a resistor to ground ($r = 5$ kΩ). The resistor r converts the current I_α out of reservoir α to a voltage signal measured by the voltage amplifier; it also converts the current from the current source to a voltage excitation V_α applied at reservoir α. The nine raw differential conductance matrix elements $\tilde{g}_{\alpha\beta} = dI_\beta/dV_\alpha$ are measured simultaneously with lock-in excitations of 20 μV_{rms} at 44, 20, and 36 Hz on reservoirs 0, 1, and 2, respectively. Subtracting r from the matrix $\tilde{\mathbf{g}}$ yields the intrinsic conductance matrix $\mathbf{g} = [\mathbf{E} + r\tilde{\mathbf{g}}]^{-1} \cdot \tilde{\mathbf{g}}$, where $\mathbf{E}$ is the identity matrix. Ohmic contact resistances ($\sim 10^3\,\Omega$) are small compared to dot resistances ($\gtrsim 10^5\,\Omega$) and are neglected in the analysis. Values for the currents I_α with bias V_0 applied to reservoir 0 are obtained by numerically integrating $\tilde{g}_{0\alpha}$.

Fluctuations in currents I_1 and I_2 are extracted from voltage fluctuations around 2 MHz across separate resistor-inductor-capacitor (RLC) resonators [Fig. 1(a)]. Power spectral densities $S_{V1,2}$ and cross-spectral density

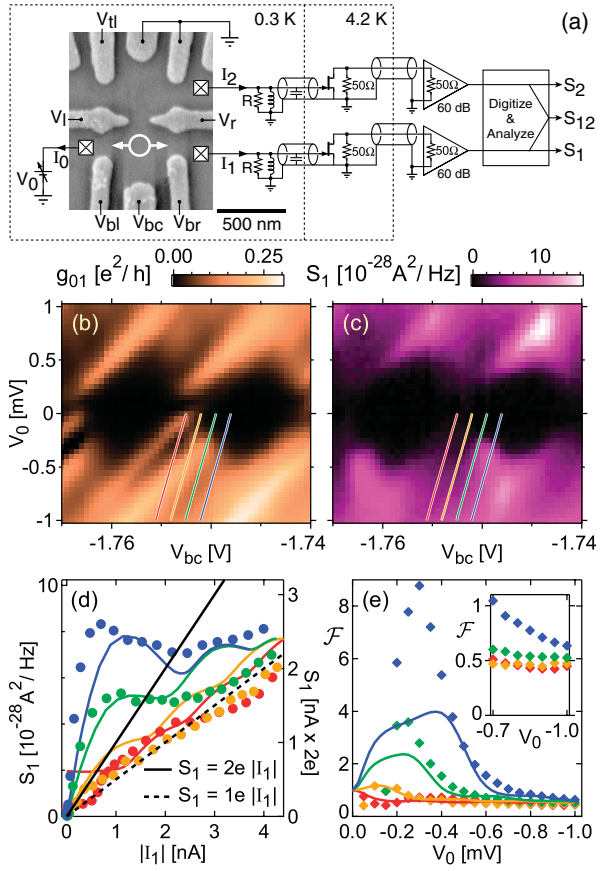

FIG. 1 (color). (a) Micrograph of the device and equivalent circuit near 2 MHz of the noise detection system (see text for equivalent circuit near dc). For the data in Figs. 1 and 2, the V_l-V_r constriction is closed and the dot is connected only to reservoirs 0 and 1. (b),(c) Differential conductance g_{01} and current noise spectral density S_1, respectively, as a function of V_0 and V_{bc}. (d) S_1 versus $|I_1|$ data (circles) and multilevel simulation (solid curves) along the four cuts indicated in (b) and (c) with corresponding colors. Black solid (dashed) line indicates $S_1 = 2e|I_1|$ ($S_1 = 1e|I_1|$). (e) Data (diamonds) and multilevel simulation (solid curves) of the modified Fano factor $\mathcal{F}$ along the same cuts as taken in (d). Inset: Detail of $\mathcal{F}$ at high $|V_0|$.

S_{V12} of these voltage fluctuations [25] are averaged over 20 s, except where noted. Following the calibration of amplifier gains and electron temperature T_e using noise thermometry [25], the dot's intrinsic current noise power spectral densities $S_{1,2}$ and cross-spectral density S_{12} are extracted by taking into account the feedback [7] and thermal noise from the finite-impedance external circuit [26].

Figure 1(b) shows conductance g_{01} as a function of V_{bc} and V_0 in a two-lead configuration, i.e., with the V_l-V_r constriction closed. The characteristic Coulomb blockade (CB) diamond structure yields a charging energy $E_C = 0.8$ meV and a lever arm for the plunger gate $\eta_{bc} = \Delta\varepsilon_d/(e\Delta V_{bc}) = 0.069$, where ε_d is the dot energy. The diamond tilt $\eta_{bc}/(1/2 - \eta_0)$ gives the lever arm for reservoir 0: $\eta_0 = \Delta\varepsilon_d/(e\Delta V_0) = 0.3$. As shown in Fig. 1(d), current noise S_1 along selected cuts close to the zero-bias CB peak (red, orange cuts) is below the Poissonian value $2e|I_1|$ at all biases $|I_1|$, while cuts that pass inside the CB diamond (green, blue cuts) exceed $2e|I_1|$ at low currents and then drop below $2e|I_1|$ at high currents. At finite T_e, the current noise $S_1^P = 2eI_1\coth(eV_0/2k_BT_e)$ of an ideal Poissonian noise source at bias V_0 may exceed $2e|I_1|$ due to the thermal (Johnson) noise contribution [9]. Accordingly, we define a modified Fano factor $\mathcal{F} \equiv S_1/S_1^P$. Figure 1(e) shows regions of super-Poissonian noise ($\mathcal{F} > 1$) when the green and blue cuts are within the CB diamond. For all cuts, $\mathcal{F}$ approaches $1/2$ at large bias.

Current noise can also be identified as sub- or super-Poissonian from the excess Poissonian noise $S_1^{EP} \equiv S_1 - S_1^P$ being negative or positive, respectively. Unlike $\mathcal{F}$, S_1^{EP} does not have divergent error bars inside the CB diamond, where currents vanish. As shown in Fig. 2(a), in regions where both I_1 and S_1 vanish, S_1^{EP} also vanishes. Far outside the CB diamonds, S_1^{EP} is negative, indicating sub-Poissonian noise. However, S_1^{EP} becomes positive along the diamond edges, indicating super-Poissonian noise in these regions.

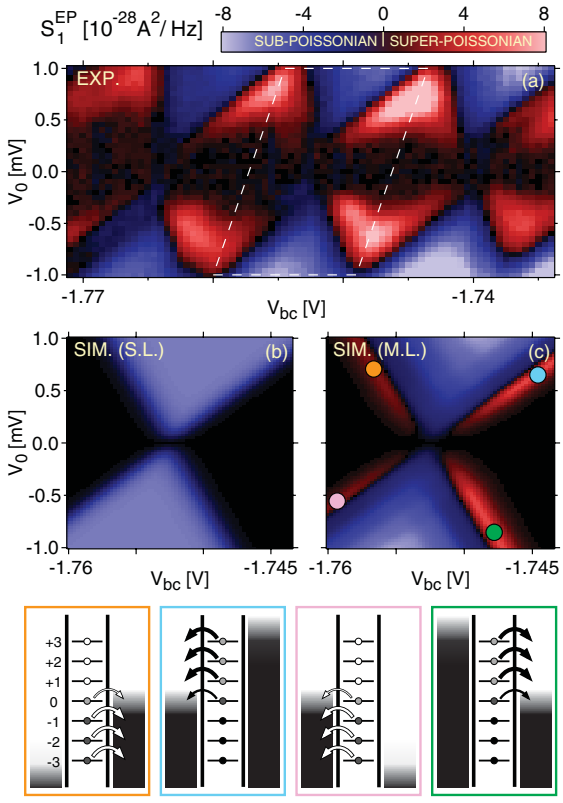

FIG. 2 (color). (a) Excess Poissonian noise S_1^{EP} as a function of V_0 and V_{bc}. Red (blue) regions indicate super- (sub-)Poissonian noise. (b),(c) Single-level (S. L.) and multilevel (M. L.) simulation of S_1^{EP}, respectively, corresponding to the data region enclosed by the white dashed parallelogram in (a). At the four colored dots superimposed on (c), where S_1^{EP} is most positive, energy diagrams are illustrated in the correspondingly colored frames at the bottom. In these diagrams, black (white) arrows indicate electron (hole) transport; the gray scale color in the reservoirs and inside the circles on each level indicates electron population, the darker the higher.

We next compare our experimental results to single-level and multilevel sequential-tunneling models of CB transport. The single-level model yields exact expressions for average current and noise [1,13,27]: $I_1 = (e/h)\int d\varepsilon \gamma_0\gamma_1(f_1 - f_0)/[(\gamma_1 + \gamma_0)^2/4 + (\varepsilon - \varepsilon_d)^2]$, $S_1 = (2e^2/h)\int d\varepsilon\{\gamma_0^2\gamma_1^2[f_0(1-f_0) + f_1(1-f_1)] + \gamma_0\gamma_1[(\gamma_1 - \gamma_0)^2/4 + (\varepsilon - \varepsilon_d)^2][f_0(1-f_1) + f_1(1-f_0)]\}/[(\gamma_1 + \gamma_0)^2/4 + (\varepsilon - \varepsilon_d)^2]^2$, where $\gamma_{0(1)}$ is the tunneling rate to reservoir 0(1) and $f_{0(1)}$ is the Fermi function in reservoir 0(1). The dot energy ε_d is controlled by gate and bias voltages: $\varepsilon_d = -eV_{\rm bc}\eta_{\rm bc} - eV_0\eta_0 - eV_1\eta_1 + \text{const}$. For the multilevel sequential-tunneling model, a master equation is used to calculate current and noise, following Refs. [11,12,28]. To model transport, we assume simple filling of orbital levels and consider transitions to and from N-electron states that differ in the occupation of at most n levels above (indexed 1 through n) and m levels below (indexed -1 through $-m$) the highest occupied level in the $(N+1)$-electron ground state (level 0) [29].

Super-Poissonian noise in the multilevel model arises from *dynamical channel blockade* [11,12], illustrated in the diagrams in Fig. 2. Consider, for example, the energy levels and transport processes shown in the green-framed diagram, which corresponds to the location of the green dot on the lower-right edge in Fig. 2(c). Along that edge, the transport involves transitions between the N-electron ground state and $(N+1)$-electron ground or excited states. When an electron occupies level 0, it will have a relatively long lifetime, as tunneling out is suppressed by the finite electron occupation in reservoir 1 at that energy. During this time, transport is blocked since the large charging energy prevents more than one non-negative-indexed level from being occupied at a time. This blockade happens dynamically during transport, leading to electron bunching and thus to super-Poissonian noise. At the location of the pink dot on the lower-left edge in Fig. 2(c), the transport involves transitions between the $(N+1)$-electron ground state and N-electron ground or excited states; a similar dynamical blockade occurs in a complementary hole transport picture. The hole transport through level 0 is slowed down by the finite hole occupation in reservoir 0, modulating the hole transport through negative-indexed levels, thus leading to hole bunching and super-Poissonian noise. Transport at the blue (orange) dot is similar to transport at the green (pink) dot but with the chemical potentials in reservoirs 0 and 1 swapped. Both experimentally and in the multilevel simulation, $S_1^{\rm EP}$ is stronger along electron edges than along hole edges. This is due to the energy dependence of the tunneling rates: since the positive-indexed electron levels have higher tunneling rates than the negative-indexed hole levels, the dynamical modulation is stronger for electron transport than for hole transport.

We next investigate the three-lead configuration, obtained by opening lead 2 [Fig. 3(a)]. At zero bias, thermal noise cross correlation is found to be in good agreement with the theoretical value [30] $S_{12} = -4k_BT_eg_{12}$, as seen in Fig. 3(b). To minimize this thermal contribution to S_{12}, output leads are subsequently tuned to weaker tunneling than the input lead ($g_{01} \sim g_{02} \sim 4g_{12}$), for reasons discussed below. Note that, as a function of $V_{\rm bc}$ and V_0, S_{12} [Fig. 3(c)] looks similar to $S_1^{\rm EP}$ [Fig. 2(a)] in the two-lead configuration [31].

Both the single-level and multilevel models can be extended to include the third lead [12,27]. Figures 3(d) and 3(e) show the single-level and multilevel simulations of S_{12}, respectively. Similar to the two-lead case, only the multilevel model reproduces the positive cross correlation along the diamond edges.

To further investigate the relationship between noise auto- and cross correlation, we compare S_{12} to the total excess Poissonian noise $S^{\rm EP} \equiv S_1 + S_2 + 2S_{12} - 2e(I_1 + I_2)\coth(eV_0/2k_BT_e)$, measured in the same three-lead configuration. Figure 4 shows $S^{\rm EP}$ and S_{12}, measured at fixed bias $V_0 = +0.5$ mV. The observed proportionality $S_{12} \sim$

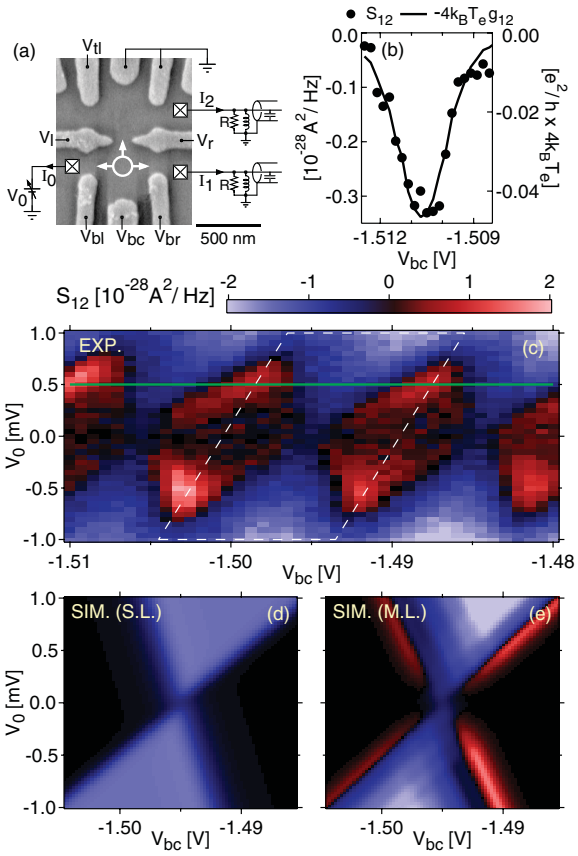

FIG. 3 (color). (a) The device in the three-lead configuration, in which the data for this figure and for Fig. 4 are taken. (b) S_{12}, integrated for 200 s, and $-4k_BT_eg_{12}$ over a CB peak at zero bias. Left and right axes are in different units but both apply to the data. (c) S_{12} as a function of V_0 and $V_{\rm bc}$. Red (blue) regions indicate positive (negative) cross correlation. (d),(e) Single-level (S.L.) and multilevel (M.L.) simulation of S_{12}, respectively, corresponding to the data region enclosed by the white dashed parallelogram in (c).

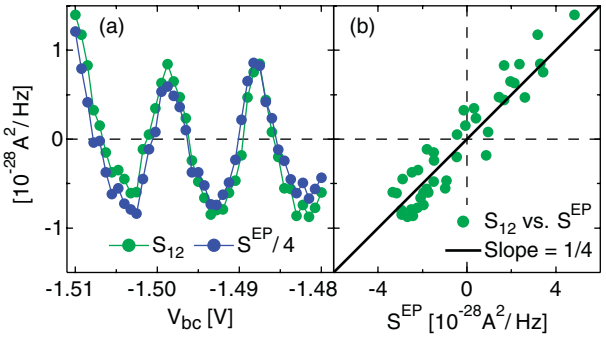

FIG. 4 (color). (a) S_{12} (green) and $S^{\mathrm{EP}}/4$ (blue) as a function of V_{bc} at $V_0 = +0.5$ mV [green horizontal line in Fig. 3(c)]. (b) Parametric plot of S_{12} (green circles) versus S^{EP} for the same data as in (a). The solid black line has a slope of $1/4$, the value expected for a 50/50 beam splitter.

$S^{\mathrm{EP}}/4$ is reminiscent of electronic HBT-type experiments [3,4,18], where noise cross correlation following a beam splitter was found to be proportional to the total output current noise in excess of the Poissonian value, with a ratio of $1/4$ for a 50/50 beam splitter. In simulation, we find that this HBT-like relationship holds in the limit $g_{01} \sim g_{02} \gg g_{12}$ (recall that $g_{01} \sim g_{02} \sim 4g_{12}$ in the experiment); on the other hand, when $g_{01} \sim g_{02} \sim g_{12}$, thermal noise gives a negative contribution that lowers S_{12} below $S^{\mathrm{EP}}/4$, as we have also observed experimentally (not shown). The implications are that first, with weak-tunneling output leads, the three-lead dot behaves as a two-lead dot followed by an ideal beam splitter, and second, the dynamical channel blockade that leads to super-Poissonian noise in the two-lead dot also gives rise to positive cross correlation in the three-lead dot.

We thank N. J. Craig for device fabrication and H.-A. Engel for valuable discussions. We acknowledge support from the NSF through the Harvard NSEC, No. PHYS 01-17795, No. DMR-05-41988, and No. DMR-0501796. M. Y. and S. T. acknowledge support from the DARPA QuIST program, the Grant-in-Aid for Scientific Research A (No. 40302799), the MEXT IT Program, and the Murata Science Foundation.

[1] Ya. M. Blanter and M. Büttiker, Phys. Rep. **336**, 1 (2000); Ya. M. Blanter, arXiv:cond-mat/0511478.
[2] M. Büttiker, Phys. Rev. Lett. **65**, 2901 (1990); M. Büttiker, Phys. Rev. B **46**, 12 485 (1992).
[3] M. Henny *et al.*, Science **284**, 296 (1999); S. Oberholzer *et al.*, Physica (Amsterdam) **6E**, 314 (2000).
[4] W. D. Oliver *et al.*, Science **284**, 299 (1999).
[5] C. Texier and M. Büttiker, Phys. Rev. B **62**, 7454 (2000).
[6] M. Büttiker, in *Quantum Noise in Mesoscopic Physics*, edited by Yu. V. Nazarov, NATO Science Series II Vol. 97 (Kluwer, Dordrecht, 2003).
[7] S.-T. Wu and S. Yip, Phys. Rev. B **72**, 153101 (2005).
[8] V. Rychkov and M. Büttiker, Phys. Rev. Lett. **96**, 166806 (2006).
[9] E. V. Sukhorukov, G. Burkard, and D. Loss, Phys. Rev. B **63**, 125315 (2001).
[10] G. Kießlich, A. Wacker, and E. Schöll, Phys. Rev. B **68**, 125320 (2003).
[11] W. Belzig, Phys. Rev. B **71**, 161301(R) (2005).
[12] A. Cottet, W. Belzig, and C. Bruder, Phys. Rev. B **70**, 115315 (2004); Phys. Rev. Lett. **92**, 206801 (2004).
[13] A. Thielmann *et al.*, Phys. Rev. Lett. **95**, 146806 (2005).
[14] G. Iannaccone *et al.*, Phys. Rev. Lett. **80**, 1054 (1998).
[15] S. S. Safonov *et al.*, Phys. Rev. Lett. **91**, 136801 (2003).
[16] Y. Chen and R. A. Webb, Phys. Rev. B **73**, 035424 (2006).
[17] P. Barthold *et al.*, Phys. Rev. Lett. **96**, 246804 (2006).
[18] Y. Chen and R. A. Webb, Phys. Rev. Lett. **97**, 066604 (2006).
[19] S. Oberholzer *et al.*, Phys. Rev. Lett. **96**, 046804 (2006).
[20] E. Onac *et al.*, Phys. Rev. Lett. **96**, 026803 (2006).
[21] S. Gustavsson *et al.*, Phys. Rev. B **74**, 195305 (2006).
[22] O. Zarchin *et al.*, Phys. Rev. Lett. **98**, 066801 (2007).
[23] D. T. McClure *et al.*, Phys. Rev. Lett. **98**, 056801 (2007).
[24] M. Eto, Jpn. J. Appl. Phys. **36**, 4004 (1997).
[25] L. DiCarlo *et al.*, Rev. Sci. Instrum. **77**, 073906 (2006).
[26] The dot's intrinsic current noises are extracted by solving the Langevin equations for finite-impedance external circuits [1]:

$$S_1 = a_{11}^2 S_{V1} + a_{21}^2 S_{V2} + 2a_{11}a_{21}S_{V12} - 4k_B T_e/R,$$
$$S_2 = a_{12}^2 S_{V1} + a_{22}^2 S_{V2} + 2a_{12}a_{22}S_{V12} - 4k_B T_e/R,$$
$$S_{12} = a_{11}a_{12}S_{V1} + a_{21}a_{22}S_{V2} + (a_{11}a_{22} + a_{12}a_{21})S_{V12},$$

where $a_{11(22)} = 1/R - g_{11(22)}$, $a_{12(21)} = -g_{12(21)}$, and R is the RLC resonator parallel resistance.
[27] H.-A. Engel, Ph.D. thesis, University of Basel, 2003.
[28] S. Hershfield *et al.*, Phys. Rev. B **47**, 1967 (1993).
[29] For computational reasons, we limit the calculation to $n = m = 3$. For simplicity, we assume equal level spacings, symmetric tunnel barriers, and an exponential dependence of the tunneling rates on level energy: $\Delta\varepsilon^l \equiv \varepsilon_d^l - \varepsilon_d^0 = l \times \delta$ and $\gamma_0^l = \gamma_1^l = \Gamma \exp(\kappa \Delta\varepsilon^l)$, where $l = -3, \ldots, 0, \ldots, 3$ is the level index, ε_d^l is the energy of level l, and $\gamma_{0(1)}^l$ is the tunneling rate from level l to reservoir 0(1). We chose $\delta = 150$ μeV, $\Gamma = 15$ GHz, and $\kappa = 0.001$ $(\mu\mathrm{eV})^{-1}$ to fit the data in Figs. 1(d) and 1(e).
[30] At zero bias, the fluctuation-dissipation theorem requires $S_{12} = -2k_B T_e(g_{12} + g_{21})$, but $g_{12} = g_{21}$ at zero bias and zero magnetic field. However, the fact that $g_{12} \neq g_{21}$ at finite bias, observed experimentally, requires knowledge of the full conductance matrix to properly extract $S_{1,2}$ and S_{12} [26].
[31] The slightly positive S_{12} ($\sim 0.2 \times 10^{-28}$ A^2/Hz) inside the rightmost diamond is due to a small drift in the residual background of S_{V12} over the 13 h of data acquisition for Fig. 3(c). Without drift, as in the shorter measurement of Fig. 3(b), S_{12} approaches 0 at zero bias as g_{12} vanishes.